ADVANCED FUNCTIONAL MATERIALS
www.afm-journal.de

Check for updates

Bulk Photovoltaic Effect in Single Ferroelectric Domain of SnS Crystal and Control of Local Polarization by Strain

*Ryo Nanae, Satsuki Kitamura, Yih-Ren Chang, Kaito Kanahashi, Tomonori Nishimura, Redhwan Moqbel, Kung-Hsuan Lin, Mina Maruyama, Yanlin Gao, Susumu Okada, Kai Qi, Jui-Han Fu, Vincent Tung, Takashi Taniguchi, Kenji Watanabe, and Kosuke Nagashio**

The bulk photovoltaic effect (BPVE) in ferroelectrics, wherein spontaneous polarization can be reversed within crystals lacking centrosymmetry, encompasses the significant contribution of ferroelectric domain walls (DWs), known as DW-PVE. Nevertheless, the separation between intrinsic BPVE within the domain and DW-PVE remains unexplored in 2D ferroelectrics, notwithstanding its significant importance. In this study, sizable crystals of 2D ferroelectric SnS are successfully grown, facilitating a comprehensive yet intricate examination of domain configurations utilizing polarized optical microscopy and piezoresponse force microscopy. By properly selecting the large ferroelectric single domain within SnS crystals, uniform intrinsic BPVE across the domain is unequivocally demonstrated. Furthermore, to further enhance intrinsic BPVE, manipulation of strain poling increased photocurrent, suggesting that locally distributed polarizations due to imperfection introduced in SnS crystals are aligned by strain. These results will offer a new avenue for rigorous comprehension of DW-PVE in 2D ferroelectrics.

1. Introduction

Ferroelectrics constitute a class of materials wherein spontaneous polarization can be reversed within crystals lacking centrosymmetry.[1] The control of ferroelectric domains has long been a subject of understanding because it forms the basis of electrical/mechanical conversion characteristics,[2] memory operation,[3] and so on in many devices. On the other hand, the phenomenon in which photovoltage is generated by light illumination in ferroelectric oxides, such as $BaTiO_3$,[4] and $LiNbO_3$,[5] was named as the bulk photovoltaic effect (BPVE) in 1957,[6] even though the origin was unclear. Unlike photovoltage generated by built-in potentials at *pn* junctions in conventional semiconductors, BPVE can achieve photovoltage greater than the bandgap (E_G) without *pn* junctions, offering significant potential[7] to surpass the Schockley-Queisser (SQ) limit.[8] Recent theoretical advancements[9–13] have proposed possible mechanisms for BPVE based on the noncentrosymmetric crystal structures, namely shift current and ballistic current. Shift current is an intrinsic mechanism where differences in Berry connection at band edges result in the shift of electron clouds in real space upon light excitation. On the

R. Nanae, S. Kitamura, K. Kanahashi, T. Nishimura, K. Nagashio
Department of Materials Engineering
The University of Tokyo
7-3-1 Hongo, Bunkyo, Tokyo 113-8656, Japan
E-mail: nagashio@material.t.u-tokyo.ac.jp

Y.-R. Chang
Nanoscale Quantum Photonics Laboratory
RIKEN Cluster for Pioneering Research
2-1 Hirosawa, Wako, Saitama 351-0198, Japan

The ORCID identification number(s) for the author(s) of this article can be found under https://doi.org/10.1002/adfm.202406140

© 2024 The Author(s). Advanced Functional Materials published by Wiley-VCH GmbH. This is an open access article under the terms of the Creative Commons Attribution-NonCommercial-NoDerivs License, which permits use and distribution in any medium, provided the original work is properly cited, the use is non-commercial and no modifications or adaptations are made.

DOI: 10.1002/adfm.202406140

R. Moqbel, K.-H. Lin
Institute of Physics
Academia Sinica
No. 128, Sec. 2, Academia Rd. Nangang Dist., Taipei 115201, Taiwan

M. Maruyama, Y. Gao, S. Okada
Department of Physics
University of Tsukuba
1-1-1 Tennodai, Tsukuba, Ibaraki 305-8571, Japan

K. Qi, J.-H. Fu, V. Tung
Department of Chemical System Engineering
The University of Tokyo
7-3-1 Hongo, Bunkyo, Tokyo 113-8656, Japan

T. Taniguchi
Research Center for Materials Nanoarchitectonics
National Institute of Materials Science
1-1 Namiki, Tsukuba, Ibaraki 305-0044, Japan

K. Watanabe
Research Center for Electronic and Optical Materials
National Institute of Materials Science
1-1 Namiki, Tsukuba, Ibaraki 305-0044, Japan

other hand, ballistic current is more extrinsic, arising from the asymmetry of photoexcitation and recombination of nonthermalized carriers. Furthermore, experimental studies controlling ferroelectric domain structures[14–16] have highlighted the substantial contribution of the domain walls (DWs) to total BPVE, in addition to intrinsic (single domain) BPVE. It has been demonstrated that above-E_G voltages can be enhanced by increasing the number of DWs. One proposed mechanism suggests that periodic potential in ferroelectric crystals with multiple domains could lead to a net potential difference when the excess charge carriers created in DWs by illumination reduce the potential in DWs.[14] Although BPVE, including DW-PVE, is attracting attention as a next-generation photovoltaic mechanism due to its potential to generate photovoltage greater than E_G and exceed the SQ limit, the wide E_G of ferroelectric oxides, such as 3.2 eV for $BaTiO_3$,[7] has impeded further harnessing of sunlight, restricting absorption to less than 10% of the solar spectrum.

In this context, 2D layered semiconductors with spontaneous polarization show promise for achieving high BPVE efficiency[17–20] because their E_G generally ranges from ≈1 to 2 eV, suitable for visible light absorption. Additionally, van der Waals stacking of different 2D materials provides a new route to manipulate their symmetry by controlling the stacking order,[21,22] even when the initial material system lacks spontaneous polarization. A fascinating example is the WS_2/black phosphorous (BP) system, where the threefold symmetry of WS_2 is disrupted by stacking with BP and in-plane electronic polarization is created at the WS_2/BP interface, leading to BPVE.[21] However, there has been limited discussion on DW-PVE in 2D materials, as the material systems studied thus far have primarily focused on (artificial) pyroelectric single crystals. Recently, BPVE has been demonstrated in out-of-plane ferroelectric $CuInP_2S_6$[23,24] and in-plane ferroelectric SnS.[25] Although ferroelectric switching has been reported for both materials,[23–28] the ferroelectric domain structures are considerably different. Atomically diffuse interfaces have been observed in $CuInP_2S_6$ from piezoresponse force microscopy (PFM) images,[23,24,29–31] whereas atomically sharp interfaces with specific atomic configurations have been reported by PFM, scanning tunneling microscopy (STM), high-angle annular dark field scanning transmission electron microscopy (HAADF-STEM) and 4D STEM in SnS[25,32] as well as in other group IV monochalcogenides like SnTe,[33–35] and SnSe.[36–38] Although the contribution of DW-PVE to BPVE is expected to vary significantly among material systems, the separation of intrinsic BPVE and DW-PVE has not yet been carried out, despite its importance for a comprehensive understanding of intrinsic BPVE.

Here, we focus on ferroelectric SnS to study intrinsic BPVE completely separated from DW-PVE because the bulk SnS has an E_G of ≈1.1 eV,[39–41] and the maximum value of the shift current tensor expected for SnS (≈100 μA/V^2) has been theoretically predicted to be comparable to that of a Si *pn* junction (250 μA/V^2),[42–44] unlike conventional perovskite oxides, which only exhibit small shift currents ($BiFeO_3$: 0.05 μA/V^2, $BaTiO_3$: 5 μA/V^2). Moreover, the curie temperature higher than room temperature of monolayer ferroelectric SnS has been experimentally confirmed,[28] and a large spontaneous electric polarization of 2.62×10^{-10} C/m has been theoretically predicted.[45] Hence, SnS holds great promise as a next-generation photovoltaic material. In this study, ferroelectric SnS crystals larger than 10 μm in size were grown on the mica substrate through physical vapor deposition (PVD) method,[46,47] enabling the observation and characterization of ferroelectric domain structure macroscopically by polarized optical microscopy (POM) and microscopically by HAADF-STEM and density functional theory (DFT), respectively. By properly selecting the large single-domain in SnS crystals, uniform intrinsic BPVE throughout the domain, separated from domain walls as well as Schottky junction, was evidently observed. Furthermore, to further enhance intrinsic BPVE, manipulation of strain poling increased photocurrent, suggesting that locally distributed polarizations due to imperfection introduced in SnS crystals are aligned by strain.

2. Results and Discussion

2.1. Material Characterization

Monolayer SnS is a multiferroic material[48,49] exhibiting ferroelectricity and ferroelasticity. The polarization switching takes place through the cubic NaCl structure from the puckered structure by the "reconnection" of the bonding under the stress or the electric field, enabling the 90° switching as well as 180°, as schematically shown in Figure S1 (Supporting Information). Two distinct stacking structures are energetically favorable,[50,51] as shown in **Figure 1**a. One represents a centrosymmetric *α* phase with AB stacking, where the spontaneous polarization cancels out, resulting in the antiferroelectric state (AB_{AFE}). The other is a noncentrosymmetric *β'* phase with AC stacking, where the spontaneous polarization aligns each other, giving rise to a robust ferroelectric state (AC_{FE}). In our previous characterization of SnS crystals grown on the mica substrate by PVD,[25,28] the metastable *β'* phase of ≈3-7 layers was stabilized at the bottom region due to substrate interaction, followed by subsequent *α* phase growth, as shown in Figure 1a. Although a thick *β'* phase is suitable to enhancing BPVE efficiency, its thickness is primarily determined by the selection of growth substrate. Hence, a crucial prerequisite is for the *α* phase to be thin to minimize unwanted light absorption, with a total thickness (t) thinner than ≈15 nm because the penetration depth of *α*-SnS is ≈20 nm for 488-nm-laser, while ensuring a large grain size for physical property measurement. Despite extensive growth studies,[46,52,53] the lateral size of SnS crystals has remained insufficient due to competition between lateral and vertical growth directions owing to the high surface reactivity of SnS associated with lone pair electrons.[54]

Recently, SnSe growth with grain sizes exceeding 20 μm has been achieved through low-pressure PVD employing extended growth periods of 2 h.[36] The primary challenge lies in mitigating nucleation rates by enhancing SnS desorption, achieved by maintaining the growth temperature as high as possible. However, after following similar growth conditions, it was realized that the surface of SnS source powders oxidized during the growth run, terminating further SnS growth. Therefore, several improvements were made to the PVD growth furnace to increase the growth time, as schematically shown in Figure 1b. (i) H_2 gas with N_2 carrier gas was introduced to maintain the reducing atmosphere, despite known reactions among SnS, SnS_2, and H_2.[55] (ii) Molecular sieves were introduced along gas lines to reduce carrier gas moisture to <100 ppb. Typical growth parameters are described in Figure S2 (Supporting Information).

© 2024 The Author(s). Advanced Functional Materials published by Wiley-VCH GmbH

16163028, 2024, 41, Downloaded from https://advanced.onlinelibrary.wiley.com/doi/10.1002/adfm.202406140 by National Institute For, Wiley Online Library on [27/04/2025]. See the Terms and Conditions (https://onlinelibrary.wiley.com/terms-and-conditions) on Wiley Online Library for rules of use; OA articles are governed by the applicable Creative Commons License

16163028, 2024, 41, Downloaded from https://advanced.onlinelibrary.wiley.com/doi/10.1002/adfm.202406140 by National Institute For, Wiley Online Library on [27/04/2025]. See the Terms and Conditions (https://onlinelibrary.wiley.com/terms-and-conditions) on Wiley Online Library for rules of use; OA articles are governed by the applicable Creative Commons License

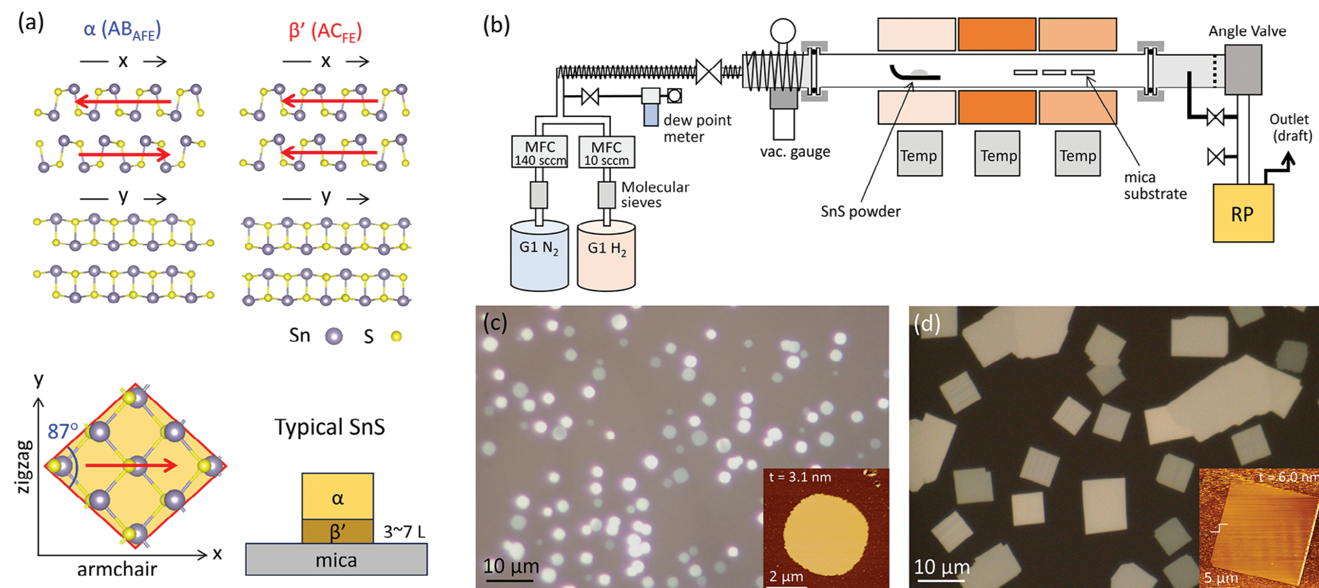

Figure 1. a) Schematic illustrations of crystal structures in the α and β' phases. The direction of polarization is shown by red arrows. Typical SnS crystals grown on the mica substrate show the β' phase formation on mica substrate and subsequent α phase formation. b) Schematic illustration of growth furnace for SnS. SnS crystals grown on the mica substrate at the growth conditions before c) and after d) the modification. Insets show AFM images of typical SnS crystals.

Following these modifications, the growth time could be extended to over 4 h, while the growth temperature was reversely increased to enhance the desorption. Atomic force microscope (AFM) and OM images of thin SnS crystals grown on the mica substrate before and after the above-mentioned modifications are compared in Figure 1c,d. It is evident that thin SnS crystals grown at 400 °C for 4 h exhibit larger grain size with thermodynamically stable crystal facets while crystals grown at 380 °C for 5 min exhibit smaller grain size with kinetically controlled shape. These characteristics were observed even for ≈5-nm-thick SnS. In this study, the largest grain size of PVD SnS with $t < 10$ nm was ≈20 µm.

With the significant increase in crystal size, a variety of bright/dark morphologies interestingly appeared via POM in reflection mode, as shown in **Figure 2a**. To confirm these as ferroelectric domains, Figure 2b compared the POM image with PFM and conductive AFM (c-AFM) images. It should be noted that this SnS crystal in Figure 2b was grown on the highly oriented pyrolytic graphite (HOPG) substrate for c-AFM. The bright/dark morphology in POM correlated with that in PFM, confirming them as ferroelectric domains. It is difficult to uniquely determine the polarization direction in in-plane SnS flake due to weak PFM sensitivity unlike out-of-plane ferroelectric materials. Moreover, in ferroelectric oxides where no electrical conduction was observed due to their insulating property, it is interesting that there is electrical conduction at the domain walls and that the difference of the electrical conduction by one order of magnitude between tail-to-tail and head-to-head domain walls is explained by the carrier accumulation and band structure change at the walls.[56–58] As SnS is a semiconductor, the difference in electrical conduction was confirmed between adjacent domains, not at the domain walls. This difference is discussed later with cross-sectional TEM observations.

To further discuss the polarization direction, POM images were captured with the parallel-polarized condition while rotating the SnS crystal, as shown in Figure 2c. Both domains A and B show twofold rotational symmetry in brightness change and were 90° shifted from each other. For materials with anisotropic dielectrics such as ferroelectrics with sufficient thickness, birefringence occurs, and the angular dependence of the intensity typically shows fourfold rotational symmetry due to the $\sin 2\theta$ term, as shown in Figure S4 (Supporting Information). On the other hand, when the crystal thickness is thinner than the wavelength of incident light, that is, the phase difference is negligible as in the present situation, the contribution of birefringence in first-order reflectance to the total reflection is negligible. Consequently, twofold rotational symmetry caused by zero-order reflectance dominates due to the $\sin\theta$ term. Furthermore, a 90° shift between two domains indicates that these domains rotate 90°/270° from each other. Based on these observations, the polarization direction in SnS crystals with stripe domain shape can be identified as a schematic image in the inset of Figure 2c. Since the 180° rotation is identical in POM, the exact polarization direction cannot be uniquely determined.

After the intensive exploration of complicated ferroelectric domain morphologies, the macroscopic shape of SnS crystals was realized to be related to the number of stripes, particularly when simple stripe domain crystals are intentionally selected. **Figure 3a** aligns POM and PFM images of the SnS crystals while increasing the number of stripes. The angle at the crystal corner is ideally 87° for the two-domain crystal, while the "macroscopic" angle of the crystal corner with an infinite number of stripes saturates to 90° with increasing the number of stripes, as schematically explained in Figure 3b. This observation suggests that the polarization direction indicated by the red arrow is indeed consistent with the armchair direction, and that the boundary

© 2024 The Author(s). Advanced Functional Materials published by Wiley-VCH GmbH

16163028, 2024, 41, Downloaded from https://advanced.onlinelibrary.wiley.com/doi/10.1002/adfm.202406140 by National Institute For, Wiley Online Library on [27/04/2025]. See the Terms and Conditions (https://onlinelibrary.wiley.com/terms-and-conditions) on Wiley Online Library for rules of use; OA articles are governed by the applicable Creative Commons License

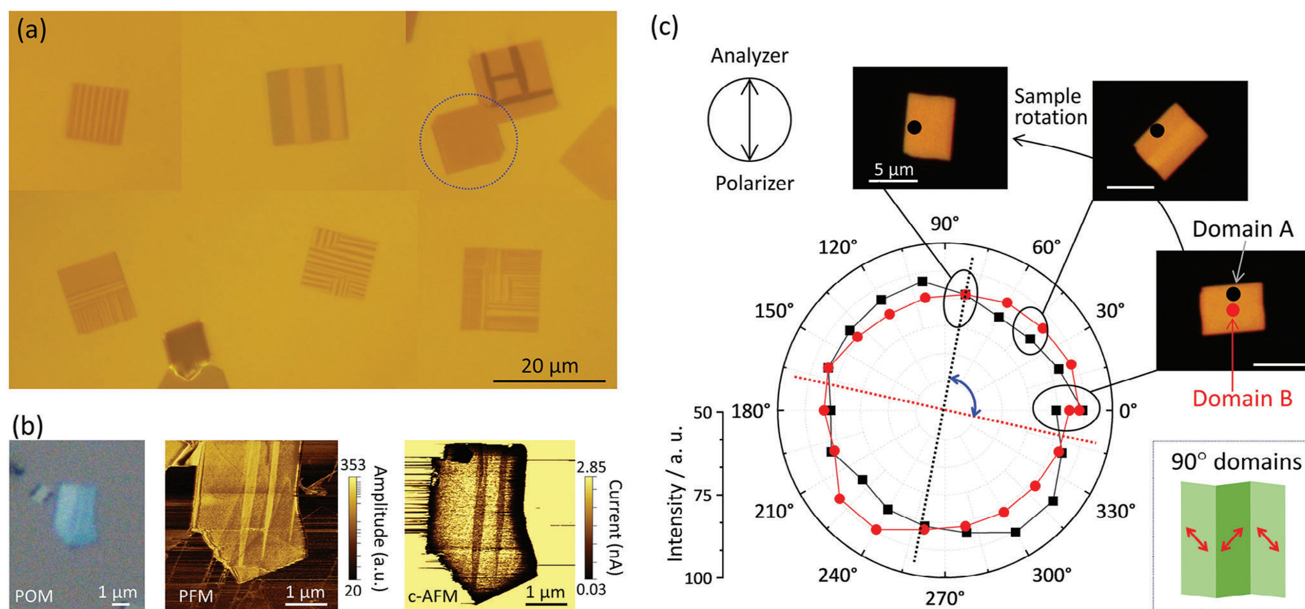

Figure 2. a) POM images of SnS crystals observed at the different place on the mica substrate. Cross-polarized condition and reflection mode was selected. b) POM, PFM, and c-AFM images of the same SnS crystal grown on the HOPG substrate. The scan direction in PFM and c-AFM is from left to right. c) POM images taken with the parallel-polarized condition while rotating the SnS crystal. Right bottom schematic in dotted box shows the identified 90° domain structure.

between 90° domains comprises the twin, as proposed in our previous study.[25] Here, our primary motivation for this observation is to identify single-domain SnS crystals for BPVE measurement. Although the SnS crystal surrounded by a blue dotted circle in Figure 2a appears to be single domain by POM, this might not be the case due to limitations in observing domain structure by POM within a certain thickness range and insufficient spatial resolution of corner angles. Therefore, two-domain SnS crystals are focused on. The PFM image in Figure 3a confirms that two domain SnS crystals do not include other small domain structures. Moreover, as shown in Figure 3c and Figure S5a (Supporting Information), scanning second harmonic generation (SHG) mapping performed on the two-domain SnS crystal also supports the single-domain structure with uniform SHG intensity shown by a red rectangular. Interestingly, another domain exhibits limited SHG intensity, suggesting that the thickness of AB stacking is much thicker than that of AC stacking (Figure 1a). This asymmetric SHG intensity of the two-domain SnS crystal has been observed in other SnS crystals and also reported in SnSe crystals.[38] Moreover, the SHG intensity in the stripe domains significantly enhanced in domains with multiple stripes, as shown in Figure S5b (Supporting Information), suggesting that the strain enhanced in the multiple domains stabilized AC stacking. As shown in Figure 3d, the cross and parallel polarization SHG polar plots of the same SnS crystal (domain with higher SHG intensity) fit well with the theoretical calculation results[59] and are in good agreement with its crystal orientation. From these results, it is now possible to identify a large single domain area in two-domain SnS crystals simply by POM. Note that the domain size in group IV monochalcogenides may depends on the structural stability,[60] for example, SnS (≈1 um), SnSe (≈100 nm),[38] and GeSe (≈50 nm).[61]

Next, the atomic structure of 90° domain walls in Figure 3b is discussed in more detail. **Figure 4a** shows two possible structures of DWs. One comprises Sn—Sn bonding with identical atomic species, which is energetically unfavorable. This is the so-called head-to-head DW (i). The other type, composed of the Sn—S bonding with dissimilar atomic species, represents an energetically favorable configuration, known as head-to-tail DW (ii). This suggested that only the head-to-tail DW structure exist within SnS DWs. To confirm this idea, cross-sectional HAADF-STEM images of DW were captured parallel to the DW to elucidate the atomic structure, as shown in Figure 4b. In the side-view atomic structure, Sn and S atoms exhibit distorted arc-shaped configurations, denoted by red and yellow shapes, depending on the projected polarization direction. The stacking sequence, analyzed through simple geometric analysis and color-coding, reveals the existence of head-to-head and tail-to-tail DWs as well as head-to-tail DWs. To justify the head-to-head structure (i), a transition region with a cubic NaCl structure is considered, as shown in (i'), because the puckered structure originates from the rupture of bonds in the cubic NaCl structure. This NaCl transition region was previously proposed in our research[25] and has recently been observed in the Bi system.[62] To comprehend the formation of this NaCl transition region, first-principles calculations for various DWs were conducted to simulate the variation in the total energy. The table in Figure 4a summarizes the relative total energies for various DWs relative to that of DW with S-Sn bonding (ii). It is evident that the average energy per length associated with Sn—Sn boding is significantly reduced to −0.196 eV Å^{-1} (i') from 0.103 eV Å^{-1} (i) upon the incorporation of the NaCl transition

 © 2024 The Author(s). Advanced Functional Materials published by Wiley-VCH GmbH

16163028, 2024, 41, Downloaded from https://advanced.onlinelibrary.wiley.com/doi/10.1002/adfm.202406140 by National Institute For, Wiley Online Library on [27/04/2025]. See the Terms and Conditions (https://onlinelibrary.wiley.com/terms-and-conditions) on Wiley Online Library for rules of use; OA articles are governed by the applicable Creative Commons License

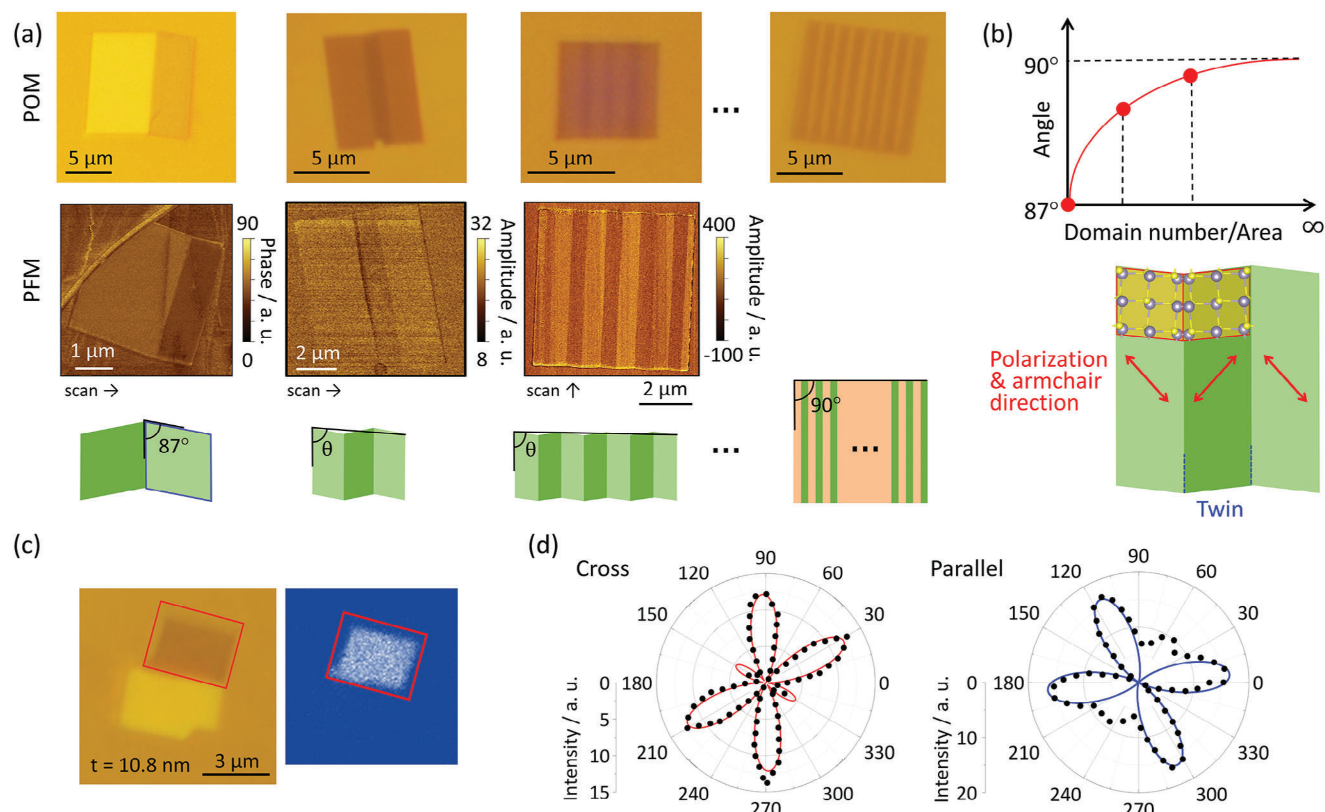

Figure 3. a) POM, PFM, and schematic drawing of domain structure as a function of the number of domain stripes. Cross-polarized condition and reflection mode was selected for POM. Note that SnS crystal for POM is different from that for PFM only for two-domain SnS crystal. The scan direction of the PFM image is shown by arrows. b) The angle at the crystal corner of the armchair direction as a function of domain number/area. The schematic drawing of three 90° domain stripes. c) OM and SHG intensity mapping. The parallel SHG condition at 180° d) The cross and parallel polarization SHG polar plots by illumination light with wavelength of 800 nm. The red and blue lines are obtained by simulating the cross and parallel polarization SHG of bulk β' SnS crystal.

region. It should be noted that the interface energies of DWs of (i) and (i') indeed represent the averages of those of Sn—Sn and S-S interfaces due to the structural model considered here. Detailed structural models and calculation methods are provided in Figure S6 (Supporting Information). However, the NaCl transition region cannot be discerned in the HAADF-STEM image due to insufficient atomic resolution resulting from the sample thickness. Despite the typical sequence of several β' layers followed by the α phase, as illustrated in Figure 1a, the present sample exhibits a complex stacking sequence with very fine domain pattern, as schematically illustrated in Figure 4b. This complexity may be attributed to the relatively large strains induced in the sample due to numerous DWs. However, as shown in c-AFM of Figure 2b, the current levels for domains with the identical polarization directions are roughly the same, suggesting the existence of a discernible rule in the layer stacking sequence.

2.2. BPVE Measurement and Strain Poling

SnS photocurrent devices were fabricated by a maskless photolithography process, as shown in Figure S7 (Supporting Information). A critical aspect involves transferring an *h*-BN flake with ≈10 nm thickness onto the SnS device to prevent oxidation or degradation during photocurrent measurements. A typical device image is presented in **Figure 5a**. Spatially-resolved photocurrent measurements were performed using a digital micromirror device (DMD) with a 0.5-µm pitch to avoid mechanical drift, as shown in Figure S8 (Supporting Information). A linearly polarized laser with a wavelength of 488 nm and a power of ≈100 µW was employed in an OM system with a laser spot size of 0.66 µm for 488 nm. For the photocurrent measurement, drain current was measured at zero drain bias and under laser illumination.

Figure 5b shows the result of line scanning photocurrent measurement under laser illumination along the black line in the OM image of the inset. Since BPVE current flows along the polarization direction, the armchair direction was macroscopically selected by using the optical image. Band bending in SnS at the metal/SnS contact separates electron-hole pairs, resulting in strong Schottky current, as evidenced at the positions of the blue circles. As identical metal electrodes were employed, the peak on the left side is positive, while it is negative on the right side. Additionally, at the center region indicated by red circle, a noticeable photocurrent peak is observed, suggesting its origin from bulk SnS crystals. To further reveal whether this photocurrent peak results from BPVE, angular-dependent photocurrent measurements were performed, as shown in Figure 5c. Since the absorbance of SnS for linearly polarized light at 488 nm is

© 2024 The Author(s). Advanced Functional Materials published by Wiley-VCH GmbH

16163028, 2024, 41, Downloaded from https://advanced.onlinelibrary.wiley.com/doi/10.1002/adfm.202406140 by National Institute For, Wiley Online Library on [27/04/2025]. See the Terms and Conditions (https://onlinelibrary.wiley.com/terms-and-conditions) on Wiley Online Library for rules of use; OA articles are governed by the applicable Creative Commons License

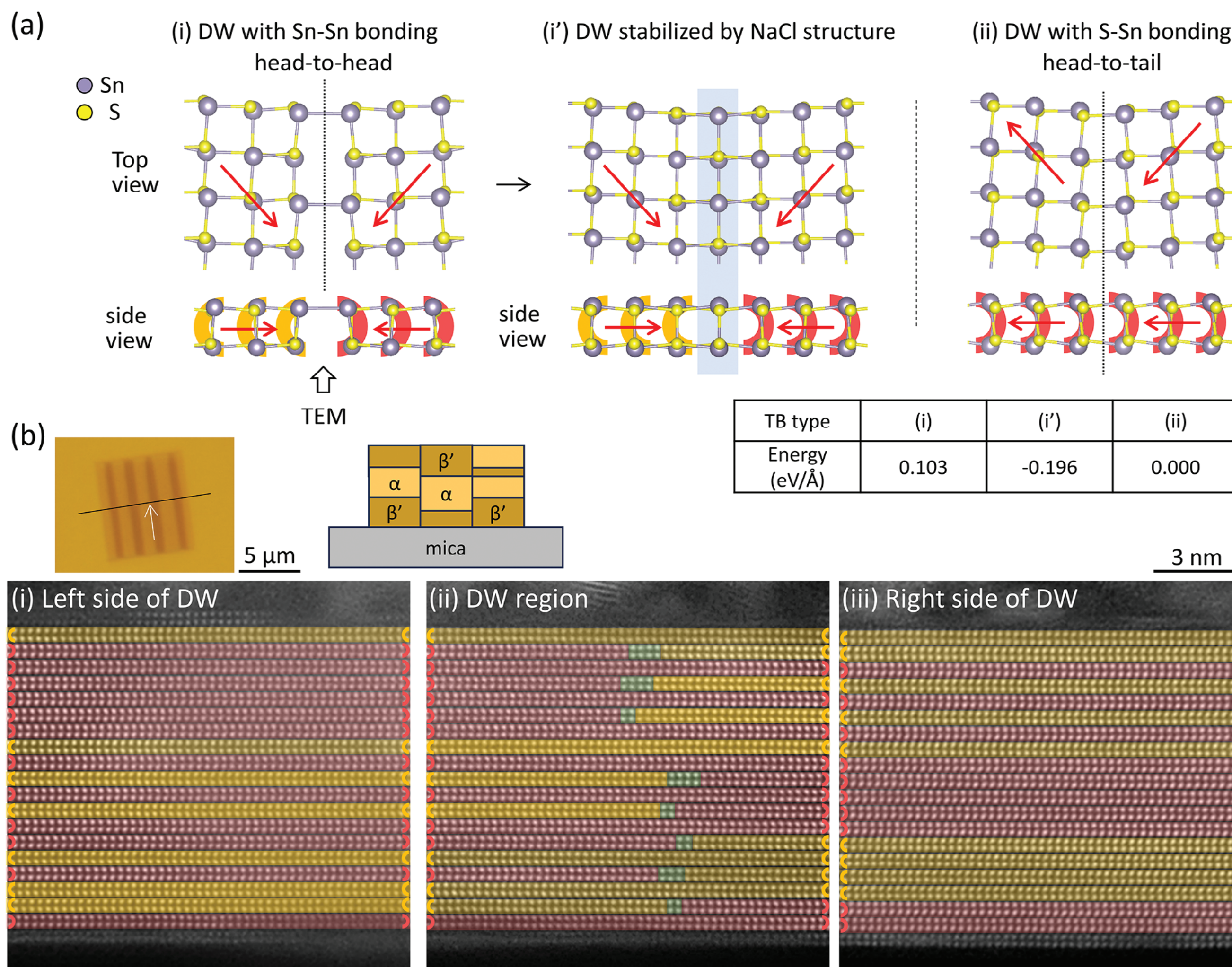

Figure 4. a) Atomic structures of two possible DWs. (i-Sn) DW with Sn—Sn bonding. (i-Sn') DW stabilized by the insertion of the cubic NaCl structure. (ii) DW with Sn—S bonding. The polarization direction in the top view and polarization direction projected in the side view are indicated by red arrows. b) Cross-sectional HAADF-STEM images of DW. (i) Left side of DW, (ii) DW region, and (iii) Right side of DW. Red and yellow hatchings denote the projected polarization directions, while green hatching represents the unclear region, expected as NaCl structure region.

nearly isotropic in all crystal directions,[63] the clear twofold rotational symmetry supports the occurrence of photocurrent due to BPVE. As SnS crystals grew larger through optimization of growth conditions, the device channel length exceeded the laser spot size. Thus, photocurrent originating from the Schottky junction, one of the primary sources of spontaneous photovoltaics, could be well separated from BPVE. On the other hand, as shown in Figure 5d, the current – voltage characteristics exhibit a similar level of photocurrents at the zero-drain bias in both armchair and zigzag directions, while the dark current is negligible for both directions. This phenomenon may be explained by the net polarization direction at the laser spot where the contribution of 90° ferroelectric domains and/or DW-PVE are included, as schematically shown in the inset of Figure 5d.

To elucidate the intrinsic BPVE without any contribution from DW-PVE, two-domain SnS crystals should be selected, as shown in Figure 3a. **Figure 6a** shows the OM image of the SnS photocurrent device where four electrodes are patterned onto the larger single domain region on the left side. The line scanning photocurrent measurement along the armchair direction in Figure 6b demonstrates uniform photocurrent contribution without any peaks, indicated by the red hatching. It should be noted that the red circle should be located at zero current if there is no BPVE current, and that this BPVE current level is comparable to that at the current peak in Figure 5b. Therefore, the uninform and flat photocurrent can be explained by the BPVE current generated in the single domain without any contribution from DW-PVE. However, the comparable level of BPVE current was observed also for the zigzag direction. In general, BPVE current along the polarization direction is much larger than that along the direction normal to the polarization direction.[64,65] Moreover, angular-dependent photocurrent measurement in Figure 6c shows nearly circular polarization dependency. Since the contribution from other domains and DW-PVE has already eliminated, another factor should be considered here. One possible origin is the poor crystallinity of the β' phase of SnS grown

 © 2024 The Author(s). Advanced Functional Materials published by Wiley-VCH GmbH

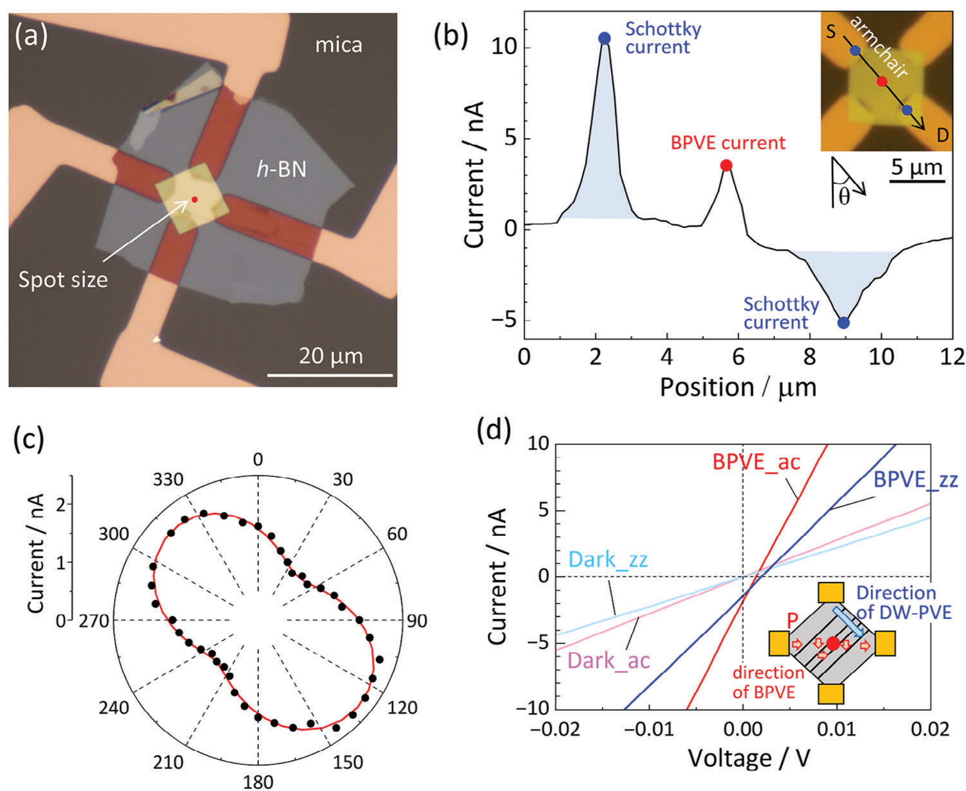

Figure 5. a) Optical micrograph of a typical SnS photocurrent device on the mica substrate. b) Photocurrent measured under zero drain bias condition along the black line in the inset. c) Angular-dependent photocurrent measured by linearly polarized light at the red circle in b). The definition of angle is shown in the inset of b). d) Current – voltage characteristics measured in armchair and zigzag directions. The inset illustrates expected domain structure.

on the mica substrate. As illustrated in Figure 6d, the polarization directions at some local areas differ from the main polarization direction along the armchair direction. This kind fluctuation in local polarization can be expected from atomic displacement or/and vacancy formation. To confirm this scenario, Raman measurements were conducted at 4 K, as shown in Figure 6e. The Raman shift at the single domain region of SnS crystal on the mica substrate clearly shows much broader peaks than that on the HOPG substrate. Moreover, for comparison at a more local area, the fast Fourier transform (FFT) of cross-sectional HAADF-STEM images of the β' phase was performed for both substrates, as shown in Figures 6f and S9 (Supporting Information). Apparently, the crystallinity of SnS on the mica substrate is poorer than that of SnS on the HOPG substrate. These results support that the intrinsic BPVE current was observed for both armchair and zigzag directions even in the single domain region.

Since SnS exhibits ferroelasticity as well as ferroelectricity, the application of strain to the SnS crystal may align polarizations pointing in different directions locally. Thus, to investigate the impact of strain on the intrinsic BPVE current, photocurrent measurement during a bending test was conducted, as shown in Figures 6g and S8 (Supporting Information). Figure S10 (Supporting Information) shows angular-dependent photocurrent measurements with increasing the strain along the armchair direction. Since plastic deformation of polyethylene terephthalate (PET) was observed at strains greater than 1%,[66] the maximum strain applied in this study was maintained below 1%. Although a clear increase in photocurrent was observed with increasing strain, various factors such as the piezoresistive effect in the β' phase, increase in E_G by tensile stress along the armchair direction, changes in Schottky barrier height at the metal/SnS contact, and others need to be taken into account under strain.[67] To simplify the experiment, as shown in Figure 6g, photocurrent was measured immediately after a single sequence of bending and relaxing, allowing all effects under strain to be released and only the effect of poling to remain. Figure 6h shows angular-dependent photocurrent measurements after releasing the strain. It is evident that the photocurrent increases with each iterative application of strain, suggesting that locally distributed polarizations are aligned by strain. It should be emphasized that the applied strain was only 1%, significantly smaller than the 4% required for ferroelastic polarization switching. This further supports the existence of locally distributed polarizations in the β' phase of SnS grown on the mica substrate. Here, it is noteworthy that strained materials, including paraelectric materials, exhibit a photovoltaic effect known as the flexo-photovoltaic effect, which displays a significant dependence on the polarization of incident light.[68–70] While it may pose a challenge to separate poling-induced polarization rearrangement from bending-induced strain gradient, the current BPVE measurements were conducted subsequent to bending and relaxation, thereby minimizing the influence of the flexo-photovoltaic effect. Consequently, it is plausible to attribute the predominant source of increased current to strain poling. Our

© 2024 The Author(s). Advanced Functional Materials published by Wiley-VCH GmbH

16163028, 2024, 41, Downloaded from https://advanced.onlinelibrary.wiley.com/doi/10.1002/adfm.202406140 by National Institute For, Wiley Online Library on [27/04/2025]. See the Terms and Conditions (https://onlinelibrary.wiley.com/terms-and-conditions) on Wiley Online Library for rules of use; OA articles are governed by the applicable Creative Commons License

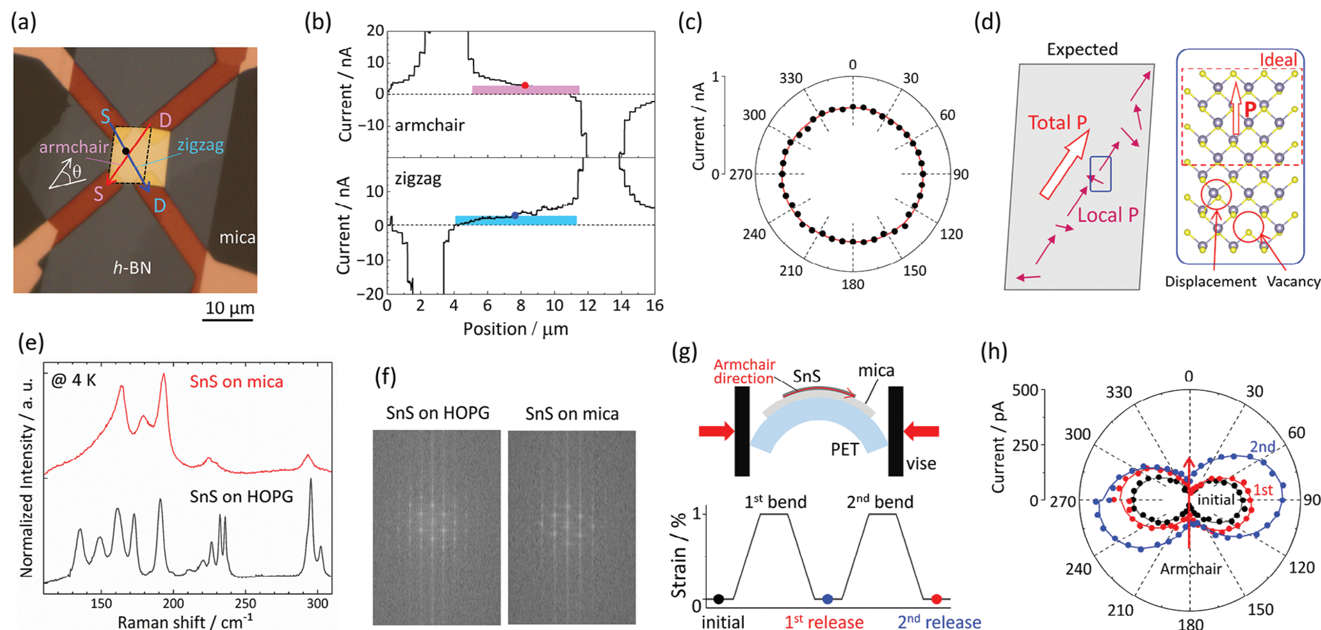

Figure 6. a) Optical micrograph of a two-domain SnS photocurrent device. b) Photocurrent measured under zero drain bias condition along the red line (top) and the blue line (bottom) in (a). c) Angular-dependent photocurrent measured by linearly polarized light at the black circle in a). The definition of angle is shown in a). d) Schematic illustration showing the locally distributed polarizations, which can originate from atomic displacement or/and vacancy formation. e) Raman spectra from the single domain region in few layer SnS on the mica substrate measured at 4 K. On the other hand, Raman spectra for SnS on the HOPG substrate were obtained for the SnS sample without identifying the domain structure since it is quite difficult to grown SnS crystals with large domains. f) the FFT of cross-sectional HAADF-STEM images of the β' phase for SnS on the mica and HOPG substrates. g) Schematic illustration of the bending test for SnS on the mica substrate. h) Angular-dependent photocurrent measured by linearly polarized light at the center of the single domain region in SnS crystal. The angle is measured from the armchair direction.

achievements on single-domain BPVE and strain poling facilitate the future advancement of BPVE research through domain engineering.

3. Conclusion

We have shown that intrinsic BPVE is uniform and flat across the single ferroelectric domain region. Furthermore, alignment of locally distributed polarizations was demonstrated by strain poling. Since intrinsic BPVE was clearly separated from DW-PVE as well as Schottky junction current, the present study paves the way for a more profound understanding of DW-PVE in 2D ferroelectrics by controlling the domain structure, proposing new perspectives for the manipulation and enhancement of BPVE in 2D materials.

4. Experimental Section

PVD Growth of SnS: A three-zone furnace with separate temperature controllers was used for the PVD growth of SnS, as schematically illustrated in Figure 1b. SnS source powder (99.9%, Kojundo Chemical Laboratory Co.) with the weight of 0.5 g was placed in zone 1, while target substrates were placed in zone 3. The tube furnace was evacuated to 10^{-2} Pa. During the growth run, a 140 sccm pure N_2 gas (99.99995%) flow was typically used as the carrier gas and 10 sccm H_2 gas (99.99999%) as reducing gas. The base pressure during the SnS growth was 60 Pa. The source temperature at zone 1 was usually set as 440 °C, while the substrate temperature at zone 3 was usually set as 400 °C. The typical growth time was 2–4 h. New surfaces of the mica substrate were obtained by cleaving with Scotch tape before every growth run. Then, the mica substrates were annealed at 400 °C for 30 min. Typical temperature profiles for SnS growth are plotted as shown in Figure S2 (Supporting information). At the end of the growth process, the furnace temperature was quenched to <100 °C within 1 min to prevent further growth.

Characterization of SnS: AFM and PFM measurements were conducted on an Asylum Research Cypher HV at room temperature in a laboratory environment. For AFM, a 42 N m^{-1} Si cantilever was used, while a 0.2 N m^{-1} conductive tip coated with Cr/Pt was used for c-AFM and PFM. For the Raman spectroscopy measurements, the SnS samples were sealed in a cryostat chamber and cooled to 4 K in a vacuum of 0.01 Torr to prevent the thermal degradation and oxidation of SnS. A semiconductor laser with a wavelength of 488 nm was applied as the incident light with a focused spot size of 1.0 μm and an incident laser power of 1 mW after passing through an objective lens (x100). The SHG analysis was conducted with a custom-built optical system under ambient conditions.[59] A mode-locked femtosecond laser with a wavelength of 800 nm was applied as the incident light source with a focused spot size of 1 μm and an incident laser power of 15–45 μW just before the samples. First-principles calculations based on density functional theory were performed for the polar plot of SHG using the OpenMX code.[71] For the cross-sectional HAADF-STEM analysis of SnS, the focused ion beam (FIB) technique was used to prepare sample cross-sections. The cross-sectional images of SnS were obtained by a JEM-ARM200F (JEOL) electron microscope at an accelerating voltage of 200 kV.

Supporting Information

Supporting Information is available from the Wiley Online Library or from the author.

© 2024 The Author(s). Advanced Functional Materials published by Wiley-VCH GmbH

16163028, 2024, 41, Downloaded from https://advanced.onlinelibrary.wiley.com/doi/10.1002/adfm.202406140 by National Institute For, Wiley Online Library on [27/04/2025]. See the Terms and Conditions (https://onlinelibrary.wiley.com/terms-and-conditions) on Wiley Online Library for rules of use; OA articles are governed by the applicable Creative Commons License

Acknowledgements

This research was supported by the JSPS KAKENHI (Grant Numbers: JP21H05237, JP21H05233, JP21H05232, JP22H04957, JP22K04212, JP22H01975, JP22KF0407, JP23K13622, JP23H00253, and JP23H02052), the NICT (Grant Number: 05901), and the JST-Mirai Program (Grant Number: JPMJMI22708192), Japan and by the National Science and Technology Council (Grant number NSTC-112-2112-M-001-073), Taiwan.

Conflict of Interest

The authors declare no conflict of interest.

Data Availability Statement

The data that support the findings of this study are available from the corresponding author upon reasonable request.

Keywords

2D materials, bulk photovoltaic effect, ferroelectric domain, group IV monochalcogenides, poling

Received: April 10, 2024
Revised: May 29, 2024
Published online: July 2, 2024

[1] M. E. Lines, A. M. Glass, *Principles and Applications of Ferroelectrics and Related Materials*, Oxford University Press, Walton Street, Oxford, **2001**.
[2] *Ferroelectric Materials for Energy Applications*, Eds: H. Huang, J. F. Scott, Wiley-VCH, Weinheim, **2019**.
[3] *Ferroelectric Random Access Memories*, Eds: H. Ishiwara, M. Okuyama, Y. Arimoto, Springer, Berlin Heidelberg, **2004**.
[4] A. G. Chynoweth, *Phys. Rev.* **1956**, *102*, 705.
[5] F. S. Chen, *J. Appl. Phys.* **1969**, *40*, 3389.
[6] J. Tauc, *Rev. Mod. Phys.* **1957**, *29*, 308.
[7] J. E. Spanier, V. M. Fridkin, A. M. Rappe, A. R. Akbashev, A. Polemi, Y. Qi, Z. Gu, S. M. Young, C. J. Hawley, D. Imbrenda, G. Xiao, A. L. Bennett-Jackson, C. L. Johnson, *Nat. Photonics* **2016**, *10*, 611.
[8] W. Shockley, H. J. Queisser, *J. Appl. Phys.* **1961**, *32*, 510.
[9] R. Von Baltz, W. Kraut, *Phys. Rev. B* **1981**, *23*, 5590.
[10] R. Resta, *Rev. Mod. Phys.* **1994**, *66*, 899.
[11] M. O. Sauer, A. Taghizadeh, U. Petralanda, M. Ovesen, K. S. Thygesen, T. Olsen, H. Cornean, T. G. Pedersen, *NPJ Comput. Mater.* **2023**, *9*, 35.
[12] T. Morimoto, N. Nagaosa, *Sci. Adv.* **2016**, *2*, 150152.
[13] Z. Dai, A. M. Rappe, *Chem. Phys. Rev.* **2023**, *4*, 011303.
[14] S. Y. Yang, J. Seidel, S. J. Byrnes, P. Shafer, C. H. Yang, M. D. Rossell, P. Yu, Y. H. Chu, J. F. Scott, J. W. Ager, L. W. Martin, R. Ramesh, *Nat. Nanotechnol.* **2010**, *5*, 143.
[15] A. Bhatnagar, A. Roy Chaudhuri, Y. Heon Kim, D. Hesse, M. Alexe, *Nat. Commun.* **2013**, *4*, 2835.
[16] R. Inoue, S. Ishikawa, R. Imura, Y. Kitanaka, T. Oguchi, Y. Noguchi, M. Miyayama, *Sci. Rep.* **2015**, *5*, 14741.
[17] Y. J. Zhang, T. Ideue, M. Onga, F. Qin, R. Suzuki, A. Zak, R. Tenne, J. H. Smet, Y. Iwasa, *Nature* **2019**, *570*, 349.
[18] D. Yang, J. Wu, B. T. Zhou, J. Liang, T. Ideue, T. Siu, K. M. Awan, K. Watanabe, T. Taniguchi, Y. Iwasa, M. Franz, Z. Ye, *Nat. Photonics* **2022**, *16*, 469.
[19] Y. Dong, M.-M. Yang, M. Yoshii, S. Matsuoka, S. Kitamura, T. Hasegawa, N. Ogawa, T. Morimoto, T. Ideue, Y. Iwasa, *Nat. Nanotechnol.* **2023**, *18*, 36.
[20] J. Wang, N. Han, Z. Lin, S. Hu, R. Tian, M. Zhang, Y. Zhang, J. Zhao, X. Gan, *Nanoscale* **2024**, *16*, 3101.
[21] T. Akamatsu, T. Ideue, L. Zhou, Y. Dong, S. Kitamura, M. Yoshii, D. Yang, M. Onga, Y. Nakagawa, K. Watanabe, T. Taniguchi, J. Laurienzo, J. Huang, Z. Ye, T. Morimoto, H. Yuan, Y. Iwasa, *Science* **2021**, *372*, 68.
[22] S. Zhang, M. Maruyama, S. Okada, M. Xue, K. Watanabe, T. Taniguchi, K. Hashimoto, Y. Miyata, R. Canton-Vitoria, R. Kitaura, *Nanoscale* **2023**, *15*, 5948.
[23] Y. Li, J. Fu, X. Mao, C. Chen, H. Liu, M. Gong, H. Zeng, *Nat. Commun.* **2021**, *12*, 5896.
[24] Y. Zhang, R. Taniguchi, S. Masubuchi, R. Moriya, K. Watanabe, T. Taniguchi, T. Sasagawa, T. Machida, *Appl. Phys. Lett.* **2022**, *120*, 013103.
[25] Y. Chang, R. Nanae, S. Kitamura, T. Nishimura, H. Wang, Y. Xiang, K. Shinokita, K. Matsuda, T. Taniguchi, K. Watanabe, K. Nagashio, *Adv. Mater.* **2023**, *35*, 2301172.
[26] L. You, Y. Zhang, S. Zhou, A. Chaturvedi, S. A. Morris, F. Liu, L. Chang, D. Ichinose, H. Funakubo, W. Hu, T. Wu, Z. Liu, S. Dong, J. Wang, *Sci. Adv.* **2019**, *5*, eaav3780.
[27] Y. Bao, P. Song, Y. Liu, Z. Chen, M. Zhu, I. Abdelwahab, J. Su, W. Fu, X. Chi, W. Yu, W. Liu, X. Zhao, Q. H. Xu, M. Yang, K. P. Loh, *Nano Lett.* **2019**, *19*, 5109.
[28] N. Higashitarumizu, H. Kawamoto, C. Lee, B. Lin, F. Chu, I. Yonemori, T. Nishimura, K. Wakabayashi, W. Chang, K. Nagashio, *Nat. Commun.* **2020**, *11*, 2428.
[29] M. Chyasnavichyus, M. A. Susner, A. V. Ievlev, E. A. Eliseev, S. V. Kalinin, N. Balke, A. N. Morozovska, M. A. McGuire, P. Maksymovych, *Appl. Phys. Lett.* **2016**, *109*, 172901.
[30] F. Liu, L. You, K. L. Seyler, X. Li, P. Yu, J. Lin, X. Wang, J. Zhou, H. Wang, H. He, S. T. Pantelides, W. Zhou, P. Sharma, X. Xu, P. M. Ajayan, J. Wang, Z. Liu, *Nat. Commun.* **2016**, *7*, 12357.
[31] D.-D. Xu, R.-R. Ma, A.-P. Fu, Z. Guan, N. Zhong, H. Peng, P.-H. Xiang, C.-G. Duan, *Nat. Commun.* **2021**, *12*, 655.
[32] P. Sutter, H. P. Komsa, H. Lu, A. Gruverman, E. Sutter, *Nano Today* **2021**, *37*, 101082.
[33] K. Chang, J. Liu, H. Lin, N. Wang, K. Zhao, A. Zhang, F. Jin, Y. Zhong, X. Hu, W. Duan, Q. Zhang, L. Fu, Q.-K. Xue, X. Chen, S.-H. Ji, *Science* **2016**, *353*, 274.
[34] K. Chang, T. P. Kaloni, H. Lin, A. Bedoya-Pinto, A. K. Pandeya, I. Kostanovskiy, K. Zhao, Y. Zhong, X. Hu, Q. K. Xue, X. Chen, S. H. Ji, S. Barraza-Lopez, S. S. P. Parkin, *Adv. Mater.* **2019**, *31*, 1804428.
[35] K. Chang, F. Küster, B. J. Miller, J. R. Ji, J. L. Zhang, P. Sessi, S. Barraza-Lopez, S. S. P. Parkin, *Nano Lett.* **2020**, *20*, 6590.
[36] M. Chiu, X. Ji, T. Zhang, N. Mao, Y. Luo, C. Shi, X. Zheng, H. Liu, Y. Han, W. L. Wilson, Z. Luo, V. Tung, J. Kong, *Adv. Electron. Mater.* **2023**, *9*, 2201031.
[37] N. Mao, Y. Luo, M. Chiu, C. Shi, X. Ji, T. S. Pieshkov, Y. Lin, H. Tang, A. J. Akey, J. A. Gardener, J. Park, V. Tung, X. Ling, X. Qian, W. L. Wilson, Y. Han, W. A. Tisdale, J. Kong, *Adv. Mater.* **2023**, *35*, 2210894.
[38] C. Shi, N. Mao, K. Zhang, T. Zhang, M. H. Chiu, K. Ashen, B. Wang, X. Tang, G. Guo, S. Lei, L. Chen, Y. Cao, X. Qian, J. Kong, Y. Han, *Nat. Commun.* **2023**, *14*, 7168.
[39] T. J. Whittles, L. A. Burton, J. M. Skelton, A. Walsh, T. D. Veal, V. R. Dhanak, *Chem. Mater.* **2016**, *28*, 3718.
[40] G. A. Tritsaris, B. D. Malone, E. Kaxiras, *J. Appl. Phys.* **2013**, *113*, 233507.
[41] L. C. Gomes, A. Carvalho, *Phys. Rev. B* **2015**, *92*, 085406.
[42] T. Rangel, B. M. Fregoso, B. S. Mendoza, T. Morimoto, J. E. Moore, J. B. Neaton, *Phys. Rev. Lett.* **2017**, *119*, 067402.
[43] H. Wang, X. Qian, *Sci. Adv.* **2019**, *5*, eaav9743.
[44] N. T. Kaner, Y. Wei, Y. Jiang, W. Li, X. Xu, K. Pang, X. Li, J. Yang, Y. Y. Jiang, G. Zhang, W. Q. Tian, *ACS Omega* **2020**, *5*, 17207.

© 2024 The Author(s). Advanced Functional Materials published by Wiley-VCH GmbH

16163028, 2024, 41, Downloaded from https://advanced.onlinelibrary.wiley.com/doi/10.1002/adfm.202406140 by National Institute For, Wiley Online Library on [27/04/2025]. See the Terms and Conditions (https://onlinelibrary.wiley.com/terms-and-conditions) on Wiley Online Library for rules of use; OA articles are governed by the applicable Creative Commons License

[45] R. Fei, W. Kang, L. Yang, *Phys. Rev. Lett.* **2016**, *117*, 097601.
[46] H. Kawamoto, N. Higashitarumizu, N. Nagamura, M. Nakamura, K. Shimamura, N. Ohashi, K. Nagashio, *Nanoscale* **2020**, *12*, 23274.
[47] Y.-R. Chang, N. Higashitarumizu, H. Kawamoto, F.-H. Chu, C.-J. Lee, T. Nishimura, R. Xiang, W.-H. Chang, S. Maruyama, K. Nagashio, *Chem. Mater.* **2021**, *33*, 186.
[48] M. Wu, X. C. Zeng, *Nano Lett.* **2016**, *16*, 3236.
[49] H. Wang, X. Qian, *2D Mater.* **2017**, *4*, 015042.
[50] A. Nalin Mehta, H. Zhang, A. Dabral, O. Richard, P. Favia, H. Bender, A. Delabie, M. Caymax, M. Houssa, G. Pourtois, W. Vandervorst, *J. Microsc.* **2017**, *268*, 276.
[51] B. Xu, J. Deng, X. Ding, J. Sun, J. Z. Liu, *NPJ Comput. Mater.* **2022**, *8*, 47.
[52] P. Sutter, E. Sutter, *ACS Appl. Nano Mater.* **2018**, *1*, 3026.
[53] E. Sutter, J. Wang, P. Sutter, *Chem. Mater.* **2020**, *32*, 8034.
[54] H. Y. Song, J. T. Lü, *Chem. Phys. Lett.* **2018**, *695*, 200.
[55] J. Felton, E. Blundo, Z. Kudrynskyi, S. Ling, J. Bradford, G. Pettinari, T. Cooper, M. Wadge, Z. Kovalyuk, A. Polimeni, P. Beton, D. Grant, G. Walker, A. Patanè, *Small* **2022**, *18*, 2202661.
[56] J. Seidel, L. W. Martin, Q. He, Q. Zhan, Y. H. Chu, A. Rother, M. E. Hawkridge, P. Maksymovych, P. Yu, M. Gajek, N. Balke, S. V. Kalinin, S. Gemming, F. Wang, G. Catalan, J. F. Scott, N. A. Spaldin, J. Orenstein, R. Ramesh, *Nat. Mater.* **2009**, *8*, 229.
[57] D. Meier, J. Seidel, A. Cano, K. Delaney, Y. Kumagai, M. Mostovoy, N. A. Spaldin, R. Ramesh, M. Fiebig, *Nat. Mater.* **2012**, *11*, 284.
[58] T. Rojac, A. Bencan, G. Drazic, N. Sakamoto, H. Ursic, B. Jancar, G. Tavcar, M. Makarovic, J. Walker, B. Malic, D. Damjanovic, *Nat. Mater.* **2017**, *16*, 322.
[59] R. Moqbel, Y.-R. Chang, Z.-Y. Li, S.-H. Kung, H.-Y. Cheng, C.-C. Lee, K. Nagashio, K.-H. Lin, *2D Mater.* **2023**, *10*, 015022.
[60] M. Mehboudi, A. M. Dorio, W. Zhu, A. Van Der Zande, H. O. H. Churchill, A. A. Pacheco-Sanjuan, E. O. Harriss, P. Kumar, S. Barraza-Lopez, *Nano Lett.* **2016**, *16*, 1704.
[61] Z. Guan, Y. Zhao, X. Wang, N. Zhong, X. Deng, Y. Zheng, J. Wang, D. Xu, R. Ma, F. Yue, Y. Cheng, R. Huang, P. Xiang, Z. Wei, J. Chu, C. Duan, *ACS Nano* **2022**, *16*, 1308.
[62] J. Gou, H. Bai, X. Zhang, Y. L. Huang, S. Duan, A. Ariando, S. A. Yang, L. Chen, Y. Lu, A. T. S. Wee, *Nature* **2023**, *617*, 67.
[63] Y. Cui, Z. Zhou, X. Wang, X. Wang, Z. Ren, L. Pan, J. Yang, *Nano Res.* **2021**, *14*, 2224.
[64] T. Noma, H. Chen, B. Dhara, M. Sotome, T. Nomoto, R. Arita, M. Nakamura, D. Miyajima, *Angew. Chem., Int. Ed.* **2023**, *62*, 202309055.
[65] M. Nakamura, S. Horiuchi, F. Kagawa, N. Ogawa, T. Kurumaji, Y. Tokura, M. Kawasaki, *Nat. Commun.* **2017**, *8*, 281.
[66] M. Umeda, N. Higashitarumizu, R. Kitaura, T. Nishimura, K. Nagashio, *Appl. Phys. Express* **2021**, *14*, 125002.
[67] I. Lee, W. T. Kang, Y. S. Shin, Y. R. Kim, U. Y. Won, K. Kim, D. L. Duong, K. Lee, J. Heo, Y. H. Lee, W. J. Yu, *ACS Nano* **2019**, *13*, 8392.
[68] J. Jiang, Z. Chen, Y. Hu, Y. Xiang, L. Zhang, Y. Wang, G. C. Wang, J. Shi, *Nat. Nanotechnol.* **2021**, *16*, 894.
[69] M. M. Yang, A. N. Iqbal, J. J. P. Peters, A. M. Sanchez, M. Alexe, *Nat. Commun.* **2019**, *10*, 2791.
[70] M. Yang, D. J. Kim, M. Alexe, *Science* **2018**, *360*, 904.
[71] The code, OpenMX, pseudoatomic basis functions, and pseudopotentials are available on the website (available at: https://www.openmx-square.org/).

 © 2024 The Author(s). Advanced Functional Materials published by Wiley-VCH GmbH

16163028, 2024, 41, Downloaded from https://advanced.onlinelibrary.wiley.com/doi/10.1002/adfm.202406140 by National Institute For, Wiley Online Library on [27/04/2025]. See the Terms and Conditions (https://onlinelibrary.wiley.com/terms-and-conditions) on Wiley Online Library for rules of use; OA articles are governed by the applicable Creative Commons License